This is a repository copy of *Mediating heat transport by microbubble dispersions: The role of dissolved gases and phase change dynamics*.

White Rose Research Online URL for this paper:
https://eprints.whiterose.ac.uk/id/eprint/230595/

Version: Published Version

Article:

Zimmerman, W.B. orcid.org/0000-0001-7123-737X (2022) Mediating heat transport by microbubble dispersions: The role of dissolved gases and phase change dynamics. Applied Thermal Engineering, 213. 118720. ISSN: 1359-4311

https://doi.org/10.1016/j.applthermaleng.2022.118720

Reuse

This article is distributed under the terms of the Creative Commons Attribution (CC BY) licence. This licence allows you to distribute, remix, tweak, and build upon the work, even commercially, as long as you credit the authors for the original work. More information and the full terms of the licence here: https://creativecommons.org/licenses/

Takedown

If you consider content in White Rose Research Online to be in breach of UK law, please notify us by emailing eprints@whiterose.ac.uk including the URL of the record and the reason for the withdrawal request.

eprints@whiterose.ac.uk
https://eprints.whiterose.ac.uk/

Applied Thermal Engineering 213 (2022) 118720

Contents lists available at ScienceDirect

Applied Thermal Engineering

journal homepage: www.elsevier.com/locate/apthermeng

Mediating heat transport by microbubble dispersions: The role of dissolved gases and phase change dynamics

William B. Zimmerman

Department of Chemical and Biological Engineering, University of Sheffield, Mappin Street, Sheffield S1 3JD, United Kingdom

ARTICLE INFO

Keywords:
Phase change energy storage
Microbubbles
Multiphase flow
Dissolved gases
Mpemba effect

ABSTRACT

Recently a theory for additional heat convection by microbubbles was posited. The mechanism proposed is that the latent heat of vapor of the liquid is carried by microbubbles from hot zones that vaporize more liquid to cold zones where condensation releases the latent heat. In this paper, the proposition that the additional heat flux is controlled by the phase fraction of microbubbles, is tested by steady state solutions of the canonical hot wall / cold wall buoyant convection problem. The simulations show that the range of additional heat transfer varies monotonically with length scale of the cavity, between 5 and 45% with phase fractions varying from 0.02 and 0.2. The larger characteristic lengths introduce insufficient heat flux from the hot wall to maintain a “driven cavity” flow structure, so that the steady state structure that emerges is a stable stratification with thin boundary layers near the hot and cold walls, with weak shear flow convection. The stable stratification resultant at higher characteristic lengths suppresses the additional heat flux due to microbubble mediation, yet only moderately deviating from proportionality. These conclusions hold qualitatively for a variant of the model which simply treats the gas exchange between the microbubble phase and dissolved gases in the liquid, resulting in variation of the microbubble phase fraction with temperature, hence with position in the domain. Quantitatively, the percentage increases are 3–30% in the parameter regime above, with the effects of dissolved gases captured dynamically.

1. Introduction

Mpemba and Osborne [1] challenged several generations of physical chemists, chemical and mechanical engineers, and physicists with a simple observation and experiments that could be carried out by high school students – how could some hot water cool faster than cold water? It had long been posited that dissolved gases in the water might be the source of this Mpemba effect, but it was not until Zimmerman [2] showed a correlation in agreement with a hypothesis about how microbubbles mediate the effect has there been any underpinning theory nor mechanistic explanation. Zimmerman [2] was aiming to demonstrate a new theory for microbubble mediated heat transfer, and found that support came from experiments already in the literature. Zimmerman [3] expands on the rationale for why only some scenarios have led to the observation of the Mpemba effect, likely due to the uncontrolled nature of the experiments. Systematic experiments such as Burridge and Linden [4] do not observe the Mpemba effect, but also aim to exclude features that would generate microbubbles with protocols that make them “systematic error.”

This paper is aimed at exploring the ability to use the new microbubble mediated model equations proposed by Zimmerman [2] for simulations that underpin engineering design, potentially applicable to several classes of unit operations where bubbles are routinely present, as well as introducing them into those where no bubble has gone before. As a scientific study, the simulations explored here can test a scaling argument that is part of Zimmerman’s [2] hypothesis for microbubble mediation of the Mpemba and Osborne [1] experiments as the dominant mechanism.

Intuitively, people understand that microbubbles should increase mass transfer due to their high surface to volume ratio, especially useful in fermentation processes (see [5]), yet they do not have the same efficacy at heat transfer due to a complication. Generally, solvents acting in unit operations where heat transfer is desirable are volatile. Additional enthalpy introduced by heating injected microbubbles is partitioned between sensible heat transfer to the liquid or to provide the latent heat for evaporation of the solvent. Microbubble distillation unit operations were developed by Zimmerman et al. [6], exploiting this possibility by observing that microbubbles achieve internal complete mixing and equilibrate with their gas-liquid interface within a few milliseconds of contact time from injection. By arranging that the liquid layer height limits the contact time to within that regime of maximum

---

E-mail address: w.zimmerman@shef.ac.uk.

https://doi.org/10.1016/j.applthermaleng.2022.118720
Received 28 January 2022; Received in revised form 4 May 2022; Accepted 20 May 2022
Available online 24 May 2022
1359-4311/© 2022 The Author. Published by Elsevier Ltd. This is an open access article under the CC BY license (http://creativecommons.org/licenses/by/4.0/).

Nomenclature

c_p	Heat capacity at constant pressure [J/kgK]
c^*	Saturation concentration [mol/m^3]
F	Latent heat density within dispersed microbubbles [J/m^3]
g,$\mathbf{g}$	Gravitational acceleration constant/vector [m/s^2]
h	Side length for 2-D square domain [m]
Gr	Non-dimensional gravity group parameter[–]
N_{Mpemba}	Dimensionless function of temperature [–]
Nu, Nu_c	Non-dimensional ratio of total to conductive heat flux [–]
p	Pressure scalar – dimensional or dimensionless (context) [N/m^2]
P^*	Saturation pressure [N/m^2]
Pr	Prandtl number (temperature dependent) [–]
q	Heat flux [W/m^2]
R	Gas constant [J/molK]
$s^*(T)$	Air or oxygen solubility in water (context) [mg / L]
T	Temperature – dimensional or dimensionless (context) [K]
t	Time coordinate [s]
$\mathbf{u}$	Velocity – dimensional or dimensionless (context) [m/s]
x	Coordinate – dimensional or dimensionless (context) [m]
z	Coordinate – dimensional or dimensionless (context) [m]

Special characters

α	Thermal diffusivity [m^2/s]
ϕ	Microbubble phase fraction [–]
k	Thermal conductivity [W/mK]
$\hat{k}$	Unit vector anti-parallel to gravity [–]
$\hat{n}$	Outward pointing unit normal to the domain [–]
ρ	Density [kg/m^3]
$\hat{\rho}$	Specific gravity (temperature dependent) [–]
μ	Dynamic viscosity [Pa·s]

Subscripts

0	Ambient or reference state

vaporization, without any time for sensible heat transfer, thermal *non-equilibrium* can be maintained with much higher vaporization rates than conventional boiling.

Desai et al. [7] is the most recent example of using microbubble distillation, also termed hot microbubble stripping, to rapidly remove ammonia from aqueous solution, achieving 100–300 fold faster processing than conventional air stripping of ammonia. Those authors also review recent advances in other applications, as well as placing the mechanism in the context of classical non-equilibrium chemical thermodynamics. Isothermal distillation is possible, which is important for thermally unstable chemical composition of the solvent or suspended materials, such as microbes, that are thermally sensitive. Many other uses in chemical and biological processing are reviewed in Gilmour and Zimmerman [5].

The new phase change dynamics theory, however, is constructive, presenting an additional exchange term / convection-like mechanism into the energy transport equation. Hence, it is in principle possible to design heat transfer devices or characterize heat transfer in unit operations, that exploit microbubble phase change mediated heat transfer. The immediate application is to direct contact heaters / condensers such as those reviewed by Ribeiro and Lage [89], but with the novel introduction of microbubbles replacing conventional fine bubbles. Similarly, bioreactors as reviewed by Gilmour and Zimmerman [5], typically have dispersed bubble phases either introduced for dosing with nutrient gases or evolved from the microbes releasing waste gases. But conventional fermenters are typically batch processes, which need to be heated during the early incubation stage, but release substantial heat during exponential growth and homeostatic production stages due to high metabolic activity, so require cooling. This additional heat transfer mechanism mediated by microbubbles, were they dispersed for either nutrient gas dosing or stripping of waste gases, could serve an additional duty for more rapid heating or cooling as required by transient metabolism of the bioculture.

Applications, however, are by no means limited to unit operations where bubbles have been previously used for heat transfer mediation in two phase contactors or known to be present. Many applications for heat transfer require cheap, even disposable, heat transfer fluids, and therefore use water. Perhaps the only widely available fluid cheaper than water is air, so the introduction of a long-lived dispersed air microbubble phase may be the least expensive intensification of heat transfer due to no need to change the infrastructure. For example, geothermal heat pumps use water as the working heat transfer fluid, but could introduce microbubbles at ground level into the cold water, which would undergo a transformation to dissolved gases with complete disappearance of the microbubble phase as it is pressurized for underground flow, and then reappearance by nucleation and cavitation as the now hot, depressurized water. In this cycle, the convection of the latent heat of vaporization from hot to cold surfaces happens while the microbubble phase exists at the lower pressures in the rising stage. This contacting pattern is very similar to the widely used deep shaft process for aerating wastewater, without, however, the pre-injection of microbubbles prior to pressurization (see Mazumder and Dikshit [10]). The injection of a long-lived microbubble phase, termed a bubble bank, whereby the microbubbles are sufficiently small that they are effectively non-buoyant but also, due to presence of surfactants or ions non-coalescent, they can remain dispersed for either longer than the processing time or potentially indefinitely, is explored by Fan et al. [11].

The new microbubble phase change theory grew from an observation of Zimmerman et al. [6] about the time scales for microbubble heat transfer response to liquid temperature change. Zimmerman [2] posited that most contacting configurations for microbubbles would achieve vapor-liquid equilibria as the contact time would naturally exceed those few milliseconds observed by Zimmerman [6]. The direct contact condenser has potential for exploitation of heat transfer by microbubbles. That paper posited an additional benefit to the obvious high gas-liquid interfacial area (therefore potential high interfacial heat transfer) and the high bubble flux (potentially hectares per cubic meter per second). Microbubbles that pass through a hot zone or near a heated surface will quickly vaporize, within milliseconds, to the saturation pressure, while absorbing the latent heat. Similarly, as they approach a cold surface or pass through a cold zone, they will condense the vapor, and release the associate latent heat.

Zimmerman [2] derived, from control volume analysis, an additional convection term for the heat transport equation. Using scaling analysis, it was deduced that the additional convective term would introduce an additional heat flux that is proportional to the microbubble phase fraction, as well as an estimate of the constant of proportionality. The hypothesis was supported by analyzing the time to freezing transient experiments of Mpemba and Osborne [1] with boiled water. The heating rates were found to correlate linearly with the inverse solubility of oxygen at the initial temperature, reflecting that the microbubble phase had equilibrated with the dissolved gas composition in the liquid. The purpose of this paper is to test whether, for steady state solutions to the canonical hot wall/cold wall problem [12], the scaling analysis of the modified heat transport equation holds, i.e. the additional heat flux is proportional to the microbubble phase fraction.

This paper is organized as follows. The novel heat transport phenomenological model is presented in Section 2, in the context of buoyant convection in a hot-wall/ cold wall canonical heat transfer configuration. This novel microbubble heat exchange term, based on phase change dynamics, although proposed in [2] and shown to be consistent in scaling predictions with [1], has never been simulated before. The Tsuji two fluid approach is adopted for the momentum equations and for the heat transport equation. Al-Mashhadani et al. [13] used this approach for mass transport phenomena, but this is the first time it has been adopted for *heat transport* with a dispersed bubble phase. The effects of microbubble phase fraction on the physical properties of the continuum phase for viscosity, density, heat capacity, and thermal conductivity turn out to be small [2], but are estimated in Section 3 for density of saturated gases.

Section 3 displays the results of this new simulation approach, and discusses them in the context of the length scale through the dimensionless gravity group ratio (Gr), which for the fixed fluid of water is controlled only by the length of the cavity side wall. In Section 4, the conclusions are drawn, including the parameter region where the proportionality between the additional heat transfer due to microbubble phase change dynamics holds.

2. Buoyant convection modelling

This section is organized as follows. The governing transport equations are presented in Section 2.1, with the novel heat transport equation incorporating the microbubble mediated phase change term introduced by [2], but not previously analysed by numerical methods. Reference [2] gave only a scaling argument. In Section 2.2, the numerical methods are described for the simulation of the governing equations in the case of the canonical hot wall / cold wall buoyant convection model, in order to evaluate the role of additional heat transport mechanism mediated by microbubbles on the emergent heat flux, as assessed by the change of the Nusselt number, for water as the working fluid. A mesh resolution study is conducted with the view to determining how well the emergent Nusselt number is estimated in the range of domains that are characterized by laminar convection, using a sufficient mesh resolution. This mesh is then adopted for all studies reported in Section 3, with the exception of those with graphical representations of detailed, distributed temperature fields and streamlines.

In Section 2.3, the range of the parametric sweep is described in terms of the controlling non-dimensional parameter, the gravity group (similar to the Galileo number), where the typical buoyant convection controlling parameters, the Prandtl and Rayleigh numbers, are dimensionless functions of temperature, because the working fluid is fixed as water. It should be noted that the model assumes that the cavity is fluid filled, which rules out Marangoni convection as a transport mechanism. The microbubble phase is assumed to be non-deformable – dispersed spheres which holds for microbubble of 100 μm diameter and smaller – so that surface tension is unimportant.

2.1. Governing transport equations

Momentum and heat transport are now a well studied area of transport phenomena, commonly coupled in computational fluid dynamics packages. The governing equations are

$$\rho\left(\frac{\partial u}{\partial t}+u\cdot\nabla u\right)=-\nabla p+\mu\nabla^2 u+\rho g$$
$$\frac{\partial\rho}{\partial t}+\nabla\cdot\rho u=0\rho c_p\left(\frac{\partial T}{\partial t}+u\cdot\nabla T\right)=\kappa\nabla^2 T \tag{1}$$

Here, the dependent variables are described as follows: $\boldsymbol{u}$ is the velocity vector, p is the pressure, and T is the temperature. The independent variables are spatial coordinates (implied in the differential operators) and time t. Everything else is a parameter (μ, ρ(T), c_p, k, g) with fixed value once the fluid and domain are defined. If there is no imposed moving boundary or pressure gradient, then motion is induced by buoyancy differences due to temperature gradients. Zimmerman [2] proposed, from control volume analysis of cycling the evaporation and condensation dynamics, a modified heat transport equation for a dispersed microbubble phase in volatile liquid. A thorough discussion of the adoption of this term is given in [2]:

$$\rho c_p\frac{DT}{Dt}=\kappa\nabla^2 T-\phi\nabla\cdot uF$$
$$=\kappa\nabla^2 T-\phi F\nabla\cdot u-\phi u\cdot(F^{'}\nabla T) \tag{2}$$

Equations (1) and (2) define a canonical problem, which with F = 0, is commonly called the hot wall / cold wall problem, used as an exemplar, for instance, for new numerical analysis methods [12]. There are two additional terms once the extra divergence term is expanded. Since the velocity field is nearly divergence free for hydrodynamics, one of the two additional terms is negligible. ϕ is the volume or phase fraction of microbubbles. *F(T)* is a state function which has the connotation of the additional energy potential that is convected by the flow representing the latent heat of vaporization for the amount of vapor (of the volatile liquid) in the dispersed microbubble phase, per unit volume:

$$F(T)=c^*(T)\Delta H_V(T)=\frac{p^*(T)}{RT}\Delta H_V(T) \tag{3}$$

$p^*(T)$ is the saturation pressure of the liquid at the absolute temperature T. For simple volatile liquids, the saturation pressure is tabulated and well correlated by the Antoine equation. *R* is the gas constant. $\Delta H_V(T)$ is the latent heat of vaporization, also commonly tabulated for volatile liquids, and commonly correlated by polynomial fit.

Equations (1) and (2) are commonly simplified by the Boussinesq approximation for buoyant convection, and non-dimensionalized by adopting scalings for length (*h*, the characteristic length scale), time ($\frac{\rho_0 c_{p,0}h^2}{\kappa}$), and velocity ($\frac{\mu_0}{\rho_0 h}$). With these scalings, the system of equations (1) modified by (2) becomes:

$$\frac{\partial u}{\partial t}+u\cdot\nabla u=-\nabla p+Pr(T)\nabla^2 u-Gr\widehat{\rho}(T)\widehat{k}$$
$$\nabla\cdot u=0 \tag{4}$$
$$\frac{DT}{Dt}=\nabla^2 T-\phi N_{Mpemba}(T)u\cdot\nabla T$$

For a small subset of our simulations, the Boussinesq approximation for the solendoidal velocity field will be replaced by the weakly compressible continuity equation $\nabla\cdot\widehat{\rho}(T)\boldsymbol{u}=0$. This will be flagged in Section 3.5 for the assessment of the validity of the Boussinesq approximation.

2.2. Numerical methods

2.2.1. Boundary conditions

The boundary conditions for momentum transport are no slip on all cavity surfaces. The boundary conditions for the upper and lower surfaces are insulated for heat transfer. The boundary condition for the hot wall (right) is fixed temperature at 100 °C. The boundary condition at the cold wall is fixed temperature at 0 °C.

In addition to the solution of the velocity field, for presentational purposes, the 2-D streamfunction is computed from the well known relationship that $\nabla^2\psi=-\omega=\frac{\partial v}{\partial x}-\frac{\partial u}{\partial y}$, with boundary condition that the boundary of the cavity is the zero streamfunction. Contours of the streamfunction, i.e. streamlines, are presented in the distributed field results, such as Fig. 1, in order to clarify the role of convection in the emergent temperature / density fields.

2.2.2. Solution methodology and convergence

The PDE engine used is Comsol Multiphysics v. 5.6, implementing the Galerkin finite element method. An exemplar solution for $Gr=2\times 10^5$ with grid convergence found by using an extremely fine mesh with 26,254 elements (236064 degrees of freedom) is shown in Fig. 1. A mesh

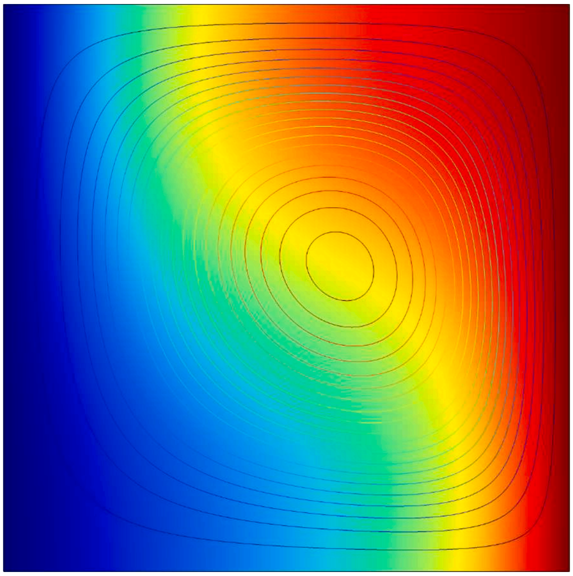

Fig. 1. Streamfunction and temperature profile for the steady state solution to (4) for water with $Gr = 2 \times 105$ (h = 1.43 mm) in the hot wall-cold wall problem on a unit square. No microbubble phase, i.e. $\phi =$ Red represents 100 °C and blue 0 °C. There are 21 streamlines, equally spaced contours of the streamfunction. (For interpretation of the references to colour in this figure legend, the reader is referred to the web version of this article.)

resolution study was conducted with a representative gravity group, $Gr = 10^{11}$, shown in Table 1. The emergent Nusselt number was unchanged to four significant digits with quadrupling the number of elements. The extremely fine mesh is used in all studies, with the exception of those reporting distributed temperature and streamfunction profiles, which use the quadrupled, finest refinement mesh described in Table 1.

Al-Mashhadani et al. [13] solved a parallel "two fluid" model for mass transfer dynamics in forced convection with injected microbubbles in airlift loop bioreactors. As illustrated in Zimmerman [14], such steady state buoyant convection problems must be solved by parametric continuation in the nonlinearity parameter $Gr = gh^3 \big/ \nu\kappa$. The approach of parametric continuation is to use the solution to the previous gravity group Gr as the initial solution for the next gravity group parameter value to be solved, at a minimum. The relative convergence tolerance is set to 10^{-6}, although nearly all solutions have relative tolerance of 10^{-12}, because the parametric solver uses as the preconditioning stiffness matrix, the converged stiffness matrix from the earlier solution.

Generally, only one Newton iteration is needed to pass the tolerance level set to 10^{-6}, by an abundant margin. For highly nonlinear problems, this methodology insures that the initial solution guess is in the basin of attraction of the Newton solver for the Galerkin finite element method implemented by Comsol Multiphysics. It also assists in the identification of bifurcation points, for which the steps in the nonlinearity parameter, say Gr here, become very small in the approach to a bifurcation point. For a "pitchfork" bifurcation, no steady solution can be found on the other side of the bifurcation, as it is unstable.

Table 1
Mesh Resolution study with $Gr = 2 \times 10^{11}$ and no microbubble phase fraction.

No. of elements	No. of degrees of freedom	Average element quality	Nusselt number
26,254	236,064	0.8692	69.2838
105,016	938,841	0.8693	69.2790

2.3. Parametric sweep for the effects of cavity size and phase fraction on emergent heat flux

For a fixed liquid, such as water, Gr has the interpretation of being controllable by changing the size of the cavity. For instance, with water, $Gr = 10^{13}$ corresponds to a side of $h = 52.7$ cm for the square domain. Typically, the parametric continuation for (4)-(5) takes 200–300 logarithmic steps to achieve $Gr \sim 10^{13}$. Because of the cubic dependence on h in Gr, for most of the parametric continuation, the hot wall-cold wall domain is very small, achieving microfluidic scales around $Gr \sim 10^{4-6}$. Fig. 1 is representative of this range.

The Prandtl number for water can be found from the NIST database of liquid properties and represented as a cubic spline interpolation function. The steady state of the model equations (4) and (5) are solved by the Galerkin finite element method for the hot wall-cold wall problem, where the hot wall is held at fixed temperature $T_1 = 373K$ and cold wall $T_0 = 273K$, on the unit square with upper and lower boundaries as no flux surfaces. This is described in Section 3.2 of Zimmerman [14] for the simpler convection situation with constant Prandtl number for water and vanishing N_{Mpemba}, defined in Fig. 2.

$\widehat{k}$ is the unit vector in the positive (antiparallel gravity) direction. $\widehat{\rho}(T)$ is the specific gravity of water, taken from Zimmerman [14] as an interpolation function via cubic splines. There are three dimensionless functions / parameters governing the dynamic similarity of the problem: (i) the Mpemba number is defined in the caption of Fig. 2, expressing the novel component of this buoyant convection analysis due to transport of the latent heat via the microbubble phase; (ii) the Prandtl number that is a function of the fluid and temperature; (iii) the buoyancy group that gives the relative importance of gravitation to dissipative mechanisms.

$$Pr(T)=\frac{\mu(T)c_p(T)}{\kappa(T)};\quad \mathrm{Gr}=\frac{\rho_0^2 c_{p,0} g h^3}{\mu_0 \kappa_0}=\frac{gh^3}{\nu_0 \alpha_0} \tag{5}$$

3. Results and discussion

This section is organized as follows. In Section 3.1, the base case of the range of cavity length scales is explored with graphical snapshots of the emergent flow regimes, particularly showing the key feature of water – the emergence of a stable stratification with the bottom stratum at approximately 4 °C, the maximum density of water – a non-Boussinesq fluid. Most buoyant convection models use a monotonic dependence of density on temperature as the equation of state, leading

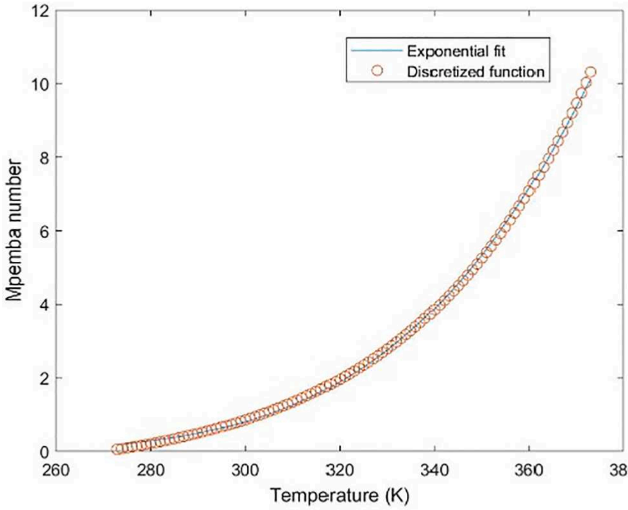

Fig. 2. $N_{Mpemba} = \frac{F'(T)}{\rho_0 c_{p,0}}$ plotted against absolute temperature for water, along with the exponential fit, where the "0" reference state are the properties of water at 20 °C. Air saturation is assumed by using the solubility curve.

to a characteristic Rayleigh number controlling the dynamics, and no emergence of a stable stratification. In Section 3.2, the role of microbubble phase fraction in varying the emergent Nusselt number is explored, with the base case of no microbubbles used to evaluate the predicted additional heat transfer flux due to the microbubble phase fraction, particularly to test whether the scaling analysis that predicts proportionality [2], holds in this scenario.

Sections 3.3-3.5 are introduced to assess some of the idealizations in the central model, equations (2). Section 3.3 explores the superficial effects on the liquid density of dissolved air if the liquid is saturated. Section 3.4 derives a simple mass transfer model that gives the principle dynamics for gas exchange due to local gas solubility dependence on local temperature, thereby either augmenting or diminishing the local microbubble phase fraction. A mass balance, assuming saturation of the dissolved gases, is implemented so that the microbubble phase fraction becomes heterogeneous and spatially dependent. Zimmerman [3] proposed this mechanism of dissolution decreases heat transfer rates while cooling, but increases them while heating, because of the direction of the microbubble phase fraction change. Section 3.5 evaluates the level of approximation in the Nusselt number emergent from the simulations due to the Boussinesq approximation, by comparison to a compressible continuity equation.

3.1. The effects of varying cavity length scale, with no microbubble phase.

Fig. 1 and Fig. 3 present a set of steady state solutions for streamlines and temperature profiles for parametric series of gravity group Gr = (2×10^6, 2×10^6, 2×10^9, 2×10^{11}, 2×10^{13}) which span the equivalent side length of millimeter to half meter scale. This parametric series is a subset of the 200–300 solutions swept so that convergence is found for each subsequent value via parametric continuation. Of course, the reason parametric continuation is necessary is that gravity group Gr is a proxy for the level of nonlinearity in the dynamics. Highly nonlinear solutions are difficult to find without starting nearby in the basin of attraction for the solution via the multidimensional Newton's method employed for iterative convergence by the PDE engine.

Fig. 1 has the equivalent topology to concentric circles for streamlines consistent with the canonical lid driven cavity problem (see Zimmerman [15]) and a temperature profile moderately different from the linear temperature gradient of pure conduction. The hot (red) regime has started to extend over the top, while the cold (blue) regime is spreading over the bottom of the domain. On average, the vertical profile is now density stably stratified, i.e. hot less dense water over cold more dense water. Fig. 3(a) continues this development with further spreading of the hot zone at the top and the cold zone at the bottom, as

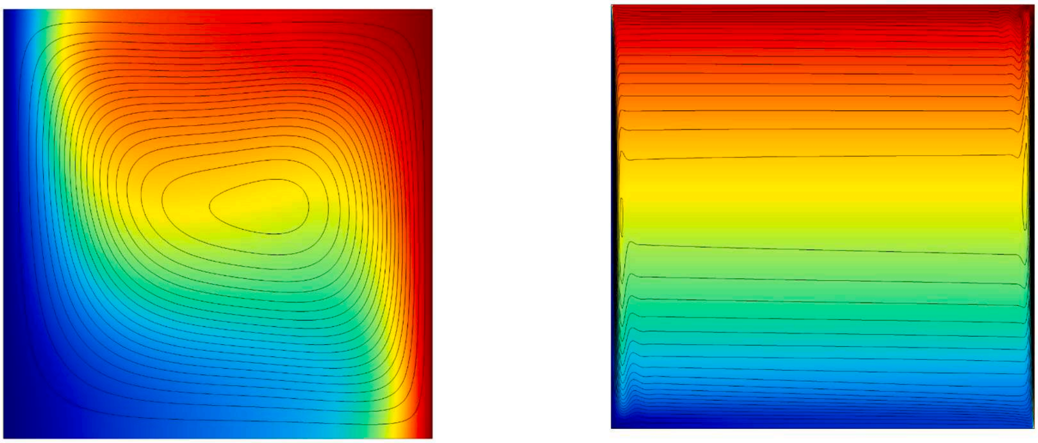

(a) ***Gr*=2 10^6**   (c) ***Gr*=2 10^{11}**

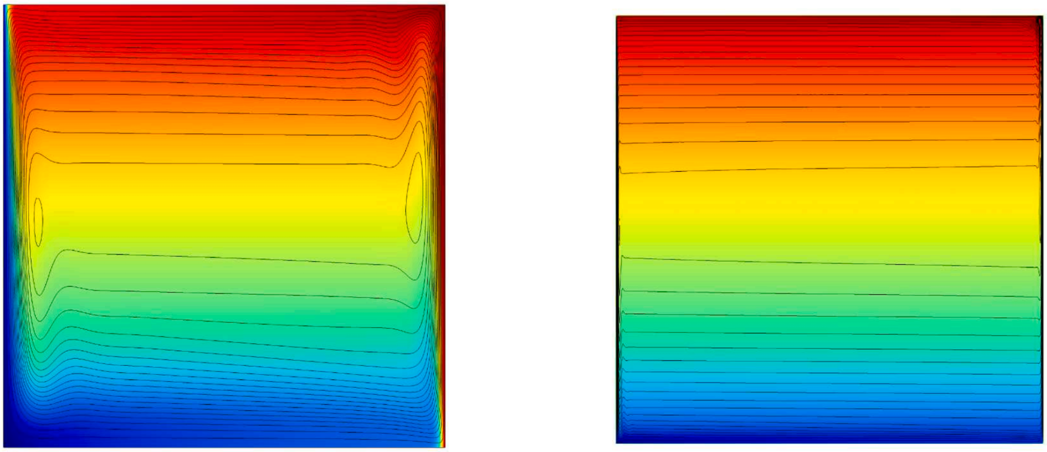

(b) ***Gr*=2 10^9**   (d) ***Gr*=2 10^{13}**

Fig. 3. Steady state solutions with a parametric series in gravity group (Gr = 2×10^6, 2×10^9, 2×10^{11}, 2×10^{13}) which can be thought of as simply changing the length of the side to (h = 3.1 mm, 3.1 cm, 14.3 cm, 66.0 cm) with ϕ = All four values of ϕ = 0, 0.02, 0.1, and 0.2 that were trialled have visually identical temperature and streamfunction profiles. Red represents T = 373 K and dark blue T = 273 K. The black streamlines are 21 uniformly spaced level sets of streamfunction from zero (the walls) to the maximum value (different in each case). (For interpretation of the references to colour in this figure legend, the reader is referred to the web version of this article.)

the streamlines become asymmetric. Fig. 3(b) shows that as Gr increases, the development of the stable stratification becomes dominant. The hot wall has a very thin boundary layer that is hot liquid, practically partitioned from the main stratified shear flow by an interposed cold layer. The wall boundary layer become thinner and thinner at the higher Gr group values in the bottom panels of Fig. 3. By Gr $\sim 10^{13}$, the stratification seems nearly total, with barely visible boundary layers near the hot and cold walls.

Simulation above Gr $\sim 10^{13}$ requires refining the mesh further, especially near the hot and cold walls to resolve the thinning boundary layers, and re-starting parametric continuation from very low Gr values – computationally expensive. Although these four simulations were conducted with $\phi = 0$, it should be noted that all four microbubble phase fractions result in visually indistinguishable flow and temperature profiles. The streamlines in the final two frames of Fig. 3 all rise along the hot wall, but then change direction, splitting off horizontally. As the flow approaches the top corner along the hot wall, the flow rapidly reverses before splitting off the upper horizontal flows. This flow reversal must be indicative of high shear rates. Seemingly the opposite dynamic occurs in the bottom left corner, but without such a rapid reversal, as the liquid layer along the bottom wall is largely a 4 °C stratum, as it is the most dense. Nonetheless, the region where liquid temperature is less than 4 °C is a very thin boundary layer along the bottom of the cold wall.

The classic textbook of Turner [16], [§7.4.3] calls this scenario convection in a slot, when the vertical walls are differentially heated. However, this canonical scenario is analyzed for a simple fluid for which density decreases monotonically with temperature, such as an ideal gas, called a Boussinesq fluid. Therefore, the Rayleigh number at fixed Prandtl number with a fixed geometry, is the controlling parameter. The qualitative description of the buoyant convective flow matches our observations with increasing gravity group *Gr*.

Our literature search has found no journal article that studies water and includes the non-Boussinesq regime around 4 °C internal density maximum in the laminar regime. Otto and Cierpka conducted the closest experimental study, focussing on laminar flow in stratified thermal energy storage systems, which for cost minimization use water as the storage liquid in general [17]. Qualitatively, the results in Fig. 3 agree with their conclusions:

> “Particle image velocimetry and temperature measurements at different heights were used obtain high-resolution vector fields of the entire wall jet flow and vertical temperature profiles… *The velocimetry shows two laminar counter-directed jets next to the vertical sidewall. In regions with high temperature gradients, the wall jets slow down, and flow reversals occur next to them…* Moreover, the wall jets are asymmetric due to temperature-dependent fluid properties in conjunction with the ambient fluid stratification. Moreover, the wall jets are asymmetric due to temperature-dependent fluid properties in conjunction with the ambient fluid stratification. In the stratification’s upper, hot part, the wall jet is thinner and faster than the bottom jet in the cold region.”

For our purposes, it is sufficient that the base simulation agree qualitatively with the literature, as the aim is to assess the additional convective heat transfer due to the microbubble phase from the base case. Ultimately, these are coupled phenomena, but quantitative validation would require experiments conducted particularly including the non-Boussinesq behaviour of water, which is of little interest to energy storage directly.

3.2. The effects of varying microbubble phase fraction.

To distinguish among the heat transfer dynamics for variation of microbubble phase fraction, some other metric than the steady state temperature profile is necessary. The common metric is the Nusselt number, which has the interpretation of the total heat transfer across a boundary relative to the conductive heat transfer. At steady state, since there is no accumulation of heat in the domain, the total heat transfer across all boundaries nets to zero. As the upper and lower boundaries are no flux boundaries, the choice to compute the Nusselt number is arbitrary between the hot and the cold wall. For convenience we take the cold wall. The Nusselt number is then defined, as applied to this geometry, is

$$Nu = \frac{\int_{\partial B} q_{tot} dS}{\int_{\partial B} q_{cond} dS} = \frac{\int_0^1 \widehat{n}\cdot\nabla T dy}{\int_0^1 \Delta T dy} = \frac{1}{T_1 - T_0}\int_0^1 \frac{\partial T}{\partial x} dy \tag{6}$$

It should be noted that the conventional definition of the Nusselt number is the ratio $Nu_c = \frac{\int_{\partial B} q_{conv} dS}{\int_{\partial B} q_{cond} dS} = \frac{\int_0^1 \widehat{n}\cdot\nabla T dy}{\int_0^1 \Delta T dy} = Nu - 1$. Here, the total heat flux is used in the definition because there are two convective terms implicit in equation (4), for which distinguishing on the boundary is not needed, nor readily achieved with user defined variables in Comsol Multiphysics, which employs intermediate terms in the finite element implementation – weak boundary terms – of Dirichlet conditions to compute the total, local heat flux more accurately than internal variables. Given that the interesting regime for human scale effects has Nu $\gg$ 1, there is little difference in using either definition.

Fig. 4 is the log-log plot of Nusselt number Nu against the gravity group Gr for four different values of microbubble phase fraction $\phi = 0$, 0.02, 0.1, and 0.2. It is clear that the heat transfer rate monotonically increases with microbubble phase fraction, as the curves are parallel, but too close to discern the variation with ϕ.This is better achieved by a relative comparison, which uses the ratio of the Nusselt number in the presence of microbubbles to the Nusselt number in absence of microbubbles, Fig. 5. Fig. 5 clarifies that the predicted scaling of the additional microbubble mediated heat flux is nearly proportional to the microbubble phase fraction for the maximum increase, which occurs in the microfluidic regime with Gr $\sim 10^6$. Thereafter, it is clear from the temperature / streamfunction profiles in Fig. 3 that the fluid becomes density stratified, with the strength of stratification increasing as Gr $\sim 10^{11}$. It is not clear from the profiles whether or not the stratification strength continues to rise above this level, as the profiles are only modestly different. The monotonic response to ϕ is apparent as the curves are non-intersecting and parallel in behavior. The maximum increases are ~5%, 13%, 25%, 30% and 45% which are close to linearly related to ϕ.

Of course, there is a rationale for why the stratification forms and then grows stronger. It is well known that in microfluidic transport, the surface area to volume of the fluid duct is very large. Zimmerman [15] analyzed the formation of stable stratification in solutions where the density is a strong function of solute concentration, including ideal solutions as well as non-ideal, even non-monotonic mixing rules. In scenarios where stirring is introduced, if the stirring is sufficiently weak, then stable stratifications form that minimize the integrated density within the domain. As the stirring rate increases, the kinetic energy can lift the solute so that a steady solution achieves greater than the minimum integrated density. In this heat transfer analogue, the stirring kinetic energy is injected proportional to the surface area of the cold wall, hence why the Nusselt number rises with increasing Gr. However, the total mass rises proportional to the volume of the duct. So eventually, the stirring force is insufficient to lift the mass to higher potential energy as Gr rises, so the temperature field (solute) is arranged to minimize the energy integral, i.e. the stable stratification suppresses convective mixing / heat transport.

The onset of the stable stratification corresponds with the maximum additional heat transfer in Fig. 5. With a fluid that does not have a non-monotonic density vs. temperature profile, [14] shows that a stable stratification does not develop at all with increasing Rayleigh number, in the laminar convection regime. We know from geophysics that ponds and lakes stratify with 4 °C water in the bottom layer, credited by biologists for the development of bacterial life, as the bottom of the pond does not freeze in winter. With low Rayeigh number (hence Gr) the flow

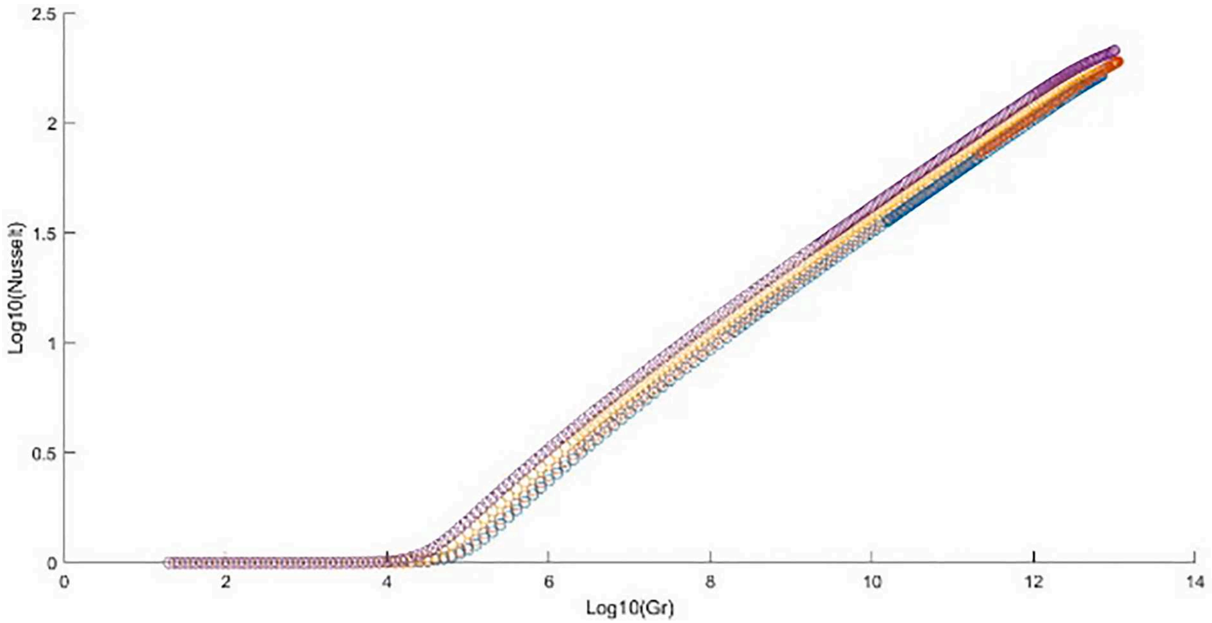

Fig. 4. Common logarithm of the Nusselt number plotted against the common logarithm of the gravity group Gr for four different values microbubble phase fraction $\phi = 0$, 0.02, 0.1, and 0.2. The lowest curve is $\phi = 0$, with Nusselt number monotonically increasing with ϕ. Because the log-log plot diminishes the distinguishability of small percentage differences in values, only this monotonic increase is a discernible trend. It should be noted that grid dependency becomes an issue for $\mathrm{Gr} > 10^{12}$, as the boundary layers near the hot and cold wall become very thin.

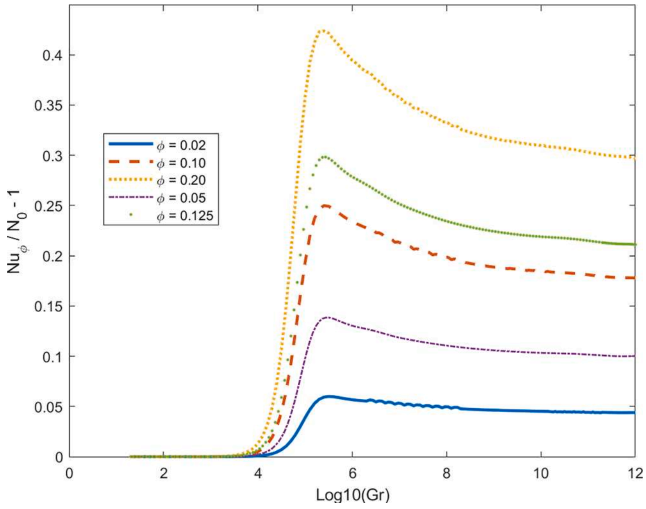

Fig. 5. Fractional change in the ratio of Nusselt numbers for ϕ relative to $\phi = 0$, plotted against the common logarithm of the gravity group Gr for three different values microbubble phase fraction $\phi = 0.02$, 0.05, 0.1, 0.125, and 0.2. The lowest curve is $\phi = 0.02$, with Nusselt number monotonically increasing with ϕ From the microfluidic scale of $\mathrm{Gr} > \sim 10^4$, the additional convective flux due to the microbubble phase rises rapidly, peaking in the millimeter scale $\mathrm{Gr} > \sim 10^6$, before plateauing with a minor decay over the next six decades, before grid dependency becomes an issue.

structure is dominated by a central convective roll. So this maximum feature should occur only if the convective roll "overshoots" with increasing Gr, what the heat transfer flux (Nusselt number) would be of the stable stratification, which suppresses convection and turbulence.

Fig. 6 makes clear that increasing ϕ increases the strength of the stable stratification as it achieves lower average specific gravity – starts the formation of the stable stratification at lower Gr values and accelerates the stabilization with increasing ϕ and Gr. This is a direct consequence of better heat transfer, as the right frame of Fig. 6 illustrates. Average temperature also rises with increasing ϕ and Gr. The microfluidic range, $\mathrm{Gr} \sim 10^{4-6}$, shows exponential increase in strength of the stable stratification / average temperature, before both level off in the millimeter scale, with a slowly rising plateau achieved in the meter scale. Zimmerman and Rees [18] studied the double diffusion problem with initial stable stratification, but strong sidewall heating. In the transient situation, the stable stratification can be overturned by sufficiently strong heating, as the stratification strength depends on solute distribution.

3.3. *The effects of density variation due to air saturation.*

Since the likelihood that the microbubble phase, upon reaching steady state, has achieved an equilibrium with the liquid, is strong, this subsection is devoted to a superficial assessment of the impact of air saturation of water, through density variation, on the emergent heat flux through the cavity walls. As the microbubble phase is persistent, after a long enough time, the liquid should be air saturated at the locally distributed temperature and one atmosphere, presuming ambient conditions outside the cavity and pressure equilibrium on the container walls.

The change in specific gravity of water due to air saturation provides the essential physical property variation to assess its impact on emergent heat flux. Watanabe and Iizuka [19] carefully measured the change in specific gravity of water with saturated, dissolved air, as a function of water temperature. Their cubic polynomial correlation was used to modify $\widehat{\rho}(T)$ for temperatures below 53 °C, the neutral change temperature (they measured between 0 and 45 °C). Oxygen and nitrogen solubility fall off dramatically above 53 °C, so there is negligible contribution above this level. This translates into a piecewise cubic polynomial modifying equations (4).

$$\Delta\widehat{\rho}(T) = \begin{cases} -5.252\times10^{-3} \;+\; 1.474\times10^{-4}T \\ \quad -\;3.0689\times10^{-6}T^2 \\ +\,4.0688\times10^{-8}T^3,\;\; T < 326K \\ \quad 0, T > 326K \end{cases} \tag{7}$$

As the average temperature in cavity the typically varies between 323 K and 332 K (cf. Fig. 6) with increasing Gr in the range explored, the

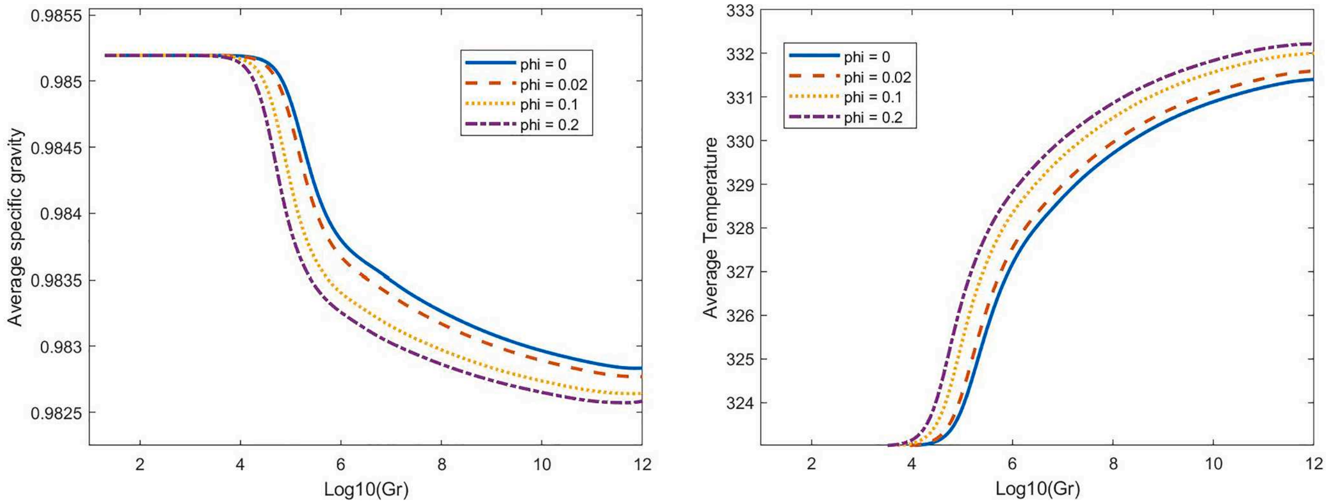

Fig. 6. (left) Volume-averaged specific density with Gr variation for selected ϕ values. (right) Volume-averaged temperature with Gr variation for selected ϕ values.

average effect of air saturation on changing density is typically around -6×10^{-4}. However, it is the spatially distributed effect that is of concern in the free convection dynamics explored here. Fig. 7 illustrates that the maximum change in Nusselt number due to the density change from air-saturation is approximately a 3% decrease, which plateaus above Gr $\sim 10^6$. However, as found for all ϕ values, the change with Nusselt number is indistinguishable visually. Compare Fig. 8 with Fig. 5 to see that there is no discernible *relative* difference to the effect of microbubble phase fraction ϕ. Zimmerman [2] argues that the thermal diffusivity increases with uniformly dispersed ϕ according to common mixing rules, but as in all length scales of interest, convection dominates the contribution to the Nusselt number, negligible effect will arise from considering the thermal diffusivity dependence on microbubble phase fraction.

This is perhaps the largest buoyancy effect that is unaccounted for in this model – the effect of the two phase density on the phase fraction of microbubbles. However, the assumption underpinning the *central* treatment in this paper is that microbubble phase fraction is uniformly distributed spatially. Undoubtedly, for any real steady state convection with dispersed microbubbles, the volume increases in warm zones and decreases in cold zones due to the vaporization and condensation, respectively. Treating these two contributions to density variation would require adding the heat transport (and consequential changes to mass transport) effects of (4) to the bubbly flow and mass transport model of [13] – beyond the scope of this paper. What can, however, be implemented fairly easily as a modification to equations (3) or (4) is an approximation to the gas exchange between the microbubble phase and dissolution in the liquid, with a strong constraint that, like thermal equilibrium between the two phases, microbubbles are instantaneously in equilibrium with their surrounding liquid, as the liquid temperature changes. The consequences of this hypothesis are explored in the next subsection.

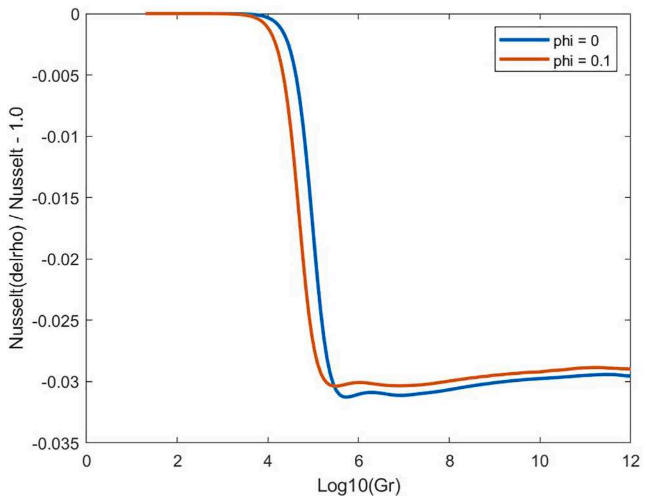

Fig. 7. Modifying the specific gravity for the air saturation of water influence according to the correlation of Watanabe and Iizuka [19]. Fractional change in the ratio of Nusselt numbers for fixed ϕ, plotted against the common logarithm of the gravity group Gr for two different values microbubble phase fraction $\phi = 0.0$, and 0.1. The lower curve is $\phi = 0$.

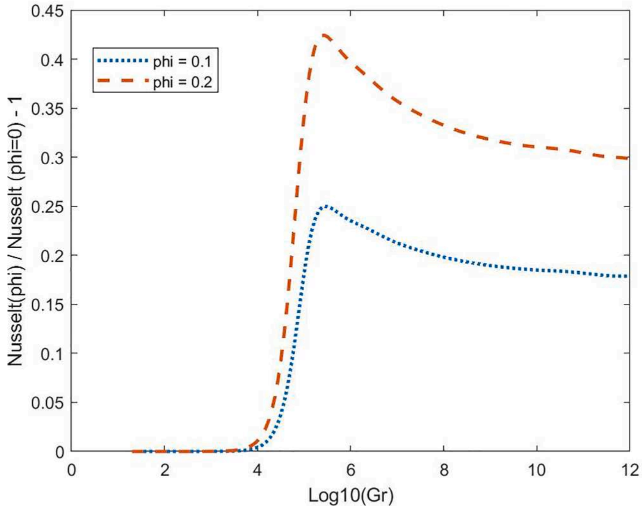

Fig. 8. Modifying the specific gravity for the air saturation of water influence according to the correlation of Watanabe and Iizuka [11]. Fractional change in the ratio of Nusselt numbers for ϕ relative to $\phi = 0$, plotted against the common logarithm of the gravity group Gr for two different values microbubble phase fraction, $\phi = 0.1$, and 0.2. The lower curve is $\phi = 0.1$.

3.4. Gas exchange between microbubbles and dissolution in the liquid

The typical approach to describing dissolved gas composition at saturation is by using Henry's Law – the partial pressure in the vapour phase in equilibrium with the concentration of the concentration in the liquid phase, which for dilute solutions is proportional, with the constant of proportionality called the Henry's Law coefficient k_H. The temperature dependence of k_H is computable from thermodynamic analysis (Karbowiak et al., [20]), giving this form for all dissolved gases in equilibrium with a gaseous phase:

$$k_H = k_H^\theta \exp\left[-\frac{\Delta_{sol}H}{R}\left(\frac{1}{T^\theta}-\frac{1}{T}\right)\right], \tag{8}$$

where R is the gas constant, $\Delta_{sol}H$ is the enthalpy change on dissolution, and the θ subscript refers to a reference temperature where k_H is known. Tromans [21] extended the chemical thermodynamics calculation of the temperature dependence to much higher temperatures than 100 °C. In general, the temperature dependence for saturated gases is very similar, which is especially true for oxygen and nitrogen, so that the shape of the curve (8) for oxygen is a proxy for air, with the absolute value well approximated by assuming a factor of 5 larger for air than oxygen.

Zimmerman [3] argues that the Engineering Toolbox [22], which provides a graph (Fig. 9) of saturated DO *s*(T)* without actually explaining the origin of the data in the database explicitly, best describes the observation that dissolved oxygen vanishes as the boiling point of water is approached. This agrees with data points of Brucker [23] drawn from Winkler titrations, a method commonly used for assessing biological activity in ecological waters and wastewaters. The Winkler method expects that the (bio)chemical composition of the water is complex, but some prior knowledge of certain components is necessary to avoid false results. The Brucker [23] dataset is limited to [0 °C, 25 °C] as that characterizes most environmental waterways, with the notable single point exception – 100 °C. The Engineering Toolbox and Brucker [23] show the *s*(T)* level achieving 0 at 100 °C, with the Engineering Toolbox showing the rapid decline in *s*(T)* in the interval [80 °C, 100 °C] as it diverges from Henry's Law temperature dependence.

Quoting the Engineering Toolbox [20]:

> "For maximum deaeration the water should be heated up to 100 °C at atmospheric pressure. This is common in steam systems where fresh water is supplied to the system through a heated deaeration tower on the top of the condensate receiver tank. It is also common to install deaeration devices on the hot sides of heat exchangers in heating distribution systems to force the dissolved air out of the system … When fresh water is heated up air bubbles start to form. The water can obviously not hold the dissolved air with increased temperature. At 100 °C water starts to boil – the bubbles are formed by evaporated water or steam. If the water is cooled down and then again reheated, bubbles will not appear until the water starts to boil. The water is deaerated."

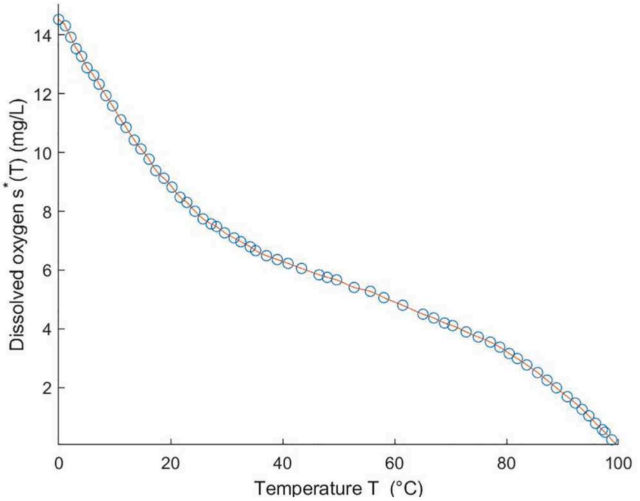

Fig. 9. Engineering Toolbox [20] solubility data for dissolved oxygen *s*(T)* in the liquid temperature range.

This is the "received wisdom" that gently raising the temperature to 100 °C deaerates, which is accord with two of the four sources of solubility data in Fig. 3. This is the first connotation of boiling (i) as described in Section 2. Burridge and Linden [4] mention that for their *ab origine* experiments they boiled the water for the purpose of partial dearation.

Dissolved gas solubility is a major unknown. Greater credence rests with the Engineering Toolbox [22] and the Winkler Method [23] as this information is experimentally driven and commonly practically applied. See Zimmerman [3].

The proposed description for the origin of additional heat transfer by dispersed microbubbles in this paper and its companions (Zimmerman [2,3]) has the virtues of being constructive and predictive. As presaged in the prior subsection, with no injection of microbubbles, a mass balance on dissolved gases and the microbubble phase fraction, presuming all the supersaturated gas migrates to the microbubble phase allows the determination of the microbubble phase fraction at a temperature T where T_{tap} is the temperature of the delivered cold tap water is found by Zimmerman [3] as

$$\phi(T) = \phi_{tap} + \left(s^*\left(T_{tap}\right) - s^*(T)\right)\frac{RT}{PM_w} \tag{9}$$

where ϕ_{tap} is the microbubble phase fraction before heating tap water. M_w is the molecular weight of the gas mixture. For convenience, $M_w = 28.97 g/mol$ is taken for air. This approach can be generalized to any initial microbubble phase fraction with forced convection of microbubbles without assuming saturation of the liquid, to

$$\phi(T) = \phi_0 - s^*(T)\frac{RT}{PM_w} \tag{10}$$

where ϕ_0 is the total initial equivalent volume fraction of air – both in the microbubble phase and dissolved in liquid water, without assuming saturation initially. Rather than treating the dynamics of mass transfer between the microbubble phase and concentration of dissolved gases as an additional transport equation, with the exchange term the explicit, this assumption allows the closure of the equations (4) with just the modification of the "Mpemba term", viz.:

$$\frac{DT}{Dt} = \nabla^2 T - \phi(T)\mathrm{N}_{\mathrm{Mpemba}}(T)\boldsymbol{u}\cdot\nabla T \tag{11}$$

In some sense, this modification is the maximum *expected deceleration* of heat transfer possible by instantaneously decreasing the microbubble phase during cooling. Zimmerman [3] gives an argument for the convolution of heat transfer and mass transfer time scales that reflects the finite time scale for mass transfer due to the laminar boundary layer between the microbubble interface and the bulk. As both heat transfer and mass transfer are the result of molecular collisions, the timescales should be comparable.

It was commented on in Section 3.1, concerning the flow and temperature profiles shown in Fig. 3 that these profile were visually indistinguishable, regardless of the variation of ϕ, yet the numerical values of the field variables themselves, as well as the Nusselt number, are dependent and sensitive to ϕ. Fig. 10 is an approach to quantifying this topological similitude for the streamfunction ψ and the temperature T fields.

Moments of a distribution are a conventional means to assess its shape. In the case of the streamfunctions, it is clear that for low gravity group values, the topology of the streamlines are concentric circles, indicative of a central maximum. The position of the central maximum can be estimated by moments of the coordinates weighted by the normalized streamfunction:

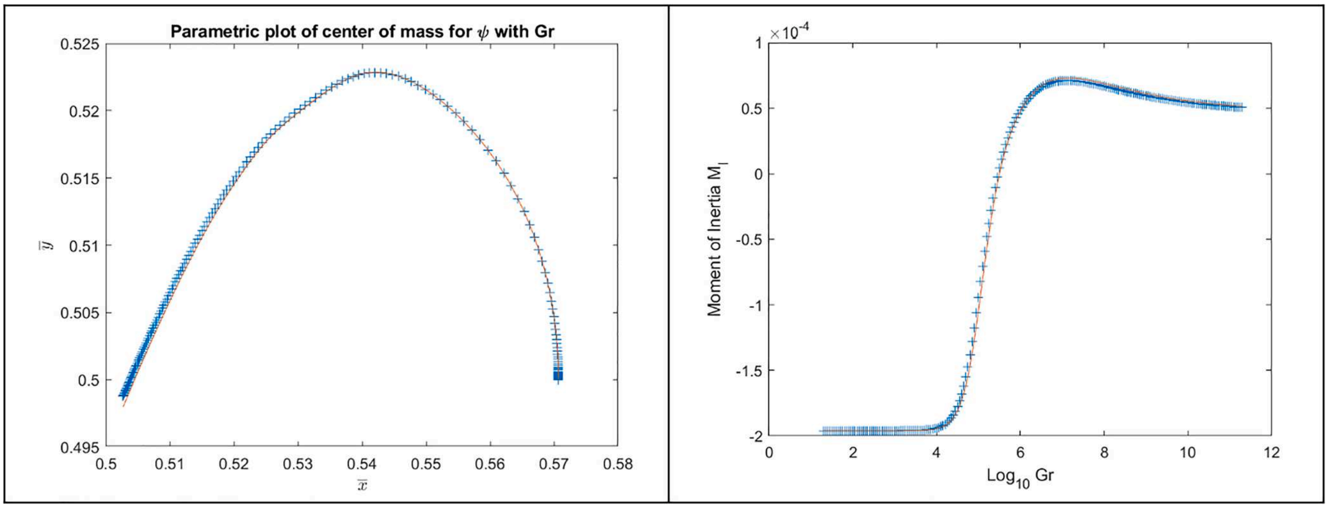

Fig. 10. (left) Parametric plot of the "center of mass" for the streamfunction ψ while varying the gravity group Gr, see equation (12). (right) The moment of inertia $\mathrm{M_I}$ defined in equation (13) variation with Gr. In both graphs, + refers to the phase fraction variation model with $\phi_0 = s^*(0^\circ C)\frac{RT}{PM_w}$, with *s*(T)* referring to saturated dissolved *air*. The solid curve is for constant microbubble phase fraction model of Section 3.1, of value $\phi = \phi_0$.

$$\begin{aligned}\bar{x} &= \frac{1}{\overline{\psi}}\int_V x\psi dV\\ \bar{y} &= \frac{1}{\overline{\psi}}\int_V y\psi dV \qquad (12)\\ \overline{\psi} &= \int_V \psi dV\end{aligned}$$

It should be noted that the streamfunction is inherently single-signed by the definition of the zero streamline as the boundary. As the streamfunction is parametrized by Gr, the global emergent values of ($\bar{x}$, $\bar{y}$) varying only with Gr. Their position, as a trajectory in Gr, is shown in the parametric plot (Fig. 10 left) for the constant microbubble phase fraction model of Section 3.1 and the temperature dependent, inhomogeneous phase fraction model of equation (10). The value of $\phi_0 = s^*(0^\circ \mathrm{C})\frac{RT}{PM_w}$ selected is the minimum value for which the model adopting (10) is physically admissible. If a lower value is selected, then saturation cannot hold throughout the temperature range of the experiment, manifesting as equation (10) resulting in a range for which the phase fraction is negative. In such a case, the simplistic dependence relying on saturation holding everywhere would require relieving to an equilibrium condition with a low temperature, sub-saturated region(s) with no microbubble phase, in the first instance.

Similarly, one can develop a notion of the non-uniformity or spread of the temperature profile to characterize its structure. Since the temperature profile results in the distribution of the mass in the constant volume domain, a candidate global emergent feature is the moment of inertia of the mass distribution, defined here as:

$$\begin{aligned}M_I &= \frac{1}{M}\int_V \left((x-0.5)^2 + (y-0.5)^2\right)\rho dV \qquad (13)\\ M &= \int_V \rho dV\end{aligned}$$

Equation (13) tacitly assumes that the center of mass for the steady state density field $\rho(T)$ is at the center of the square domain. Whether or not this holds, however, is immaterial to the interpretation that $\mathrm{M_I}$ defined so defined is a global measure of the spread of the density profile. That the moment of inertia follows a universal curve for a given "average" ϕ, irrespective of the two models for phase fraction dependency, re-inforces the universality of the topological transformations mapped out by Gr, with merely position on the trajectory dependent on the model and actual value of Gr.

It should be noted that the additional Nusselt number follows the linearity approximation to ϕ_0 proposed by Zimmerman [2] for its maximum value, with "near" linear behaviour the additional Nusselt number for higher Gr.

It is not clear how to compare the two models. Undoubtedly, the additional heat transfer of the constant ϕ model of Section 3.1 should be higher than that of the temperature dependent microbubble phase fraction of Section 3.2. Only in the very highest temperature domain does $\phi \sim \phi_0$. So, given the sign of the additional heat convection mechanism due to phase change in (11), in colder regions, there would be expected to be less additional heat transfer from this mechanism. One candidate is to approximate the appropriate $\phi \sim \phi(\overline{T})$ for comparing the two models. The average temperature, however, is dependent on Gr in both models, so one phase fraction ϕ_0 is insufficient to be "comparable" for the entire parameter space of Gr, in the laminar regime.

Fig. 12 is one attempt to bracket the dissolved gas / microbubble exchange model for $\phi \sim \phi(\overline{T})$ with two values of the constant microbubble phase fraction model. $\phi = 0.0284$ is the low Gr approximation to $\phi \sim \phi(\overline{T})$. $\phi = 0.0316$ is the high Gr value approximation, when $\phi_0 =$

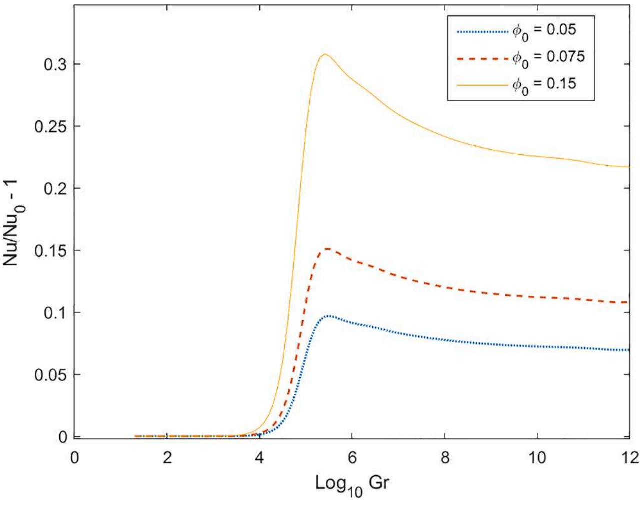

Fig. 11. The analogous graphic to Fig. 5 of Section 3.1 for the additional Nusselt number due to free convection with increasing gravity group Gr and three values of ϕ_0, which has the interpretation of the microbubble phase fraction at sufficiently high temperature that the dissolved gases have evolved into the microbubble phase, with no dissolution, i.e. 100 °C in Fig. 9.

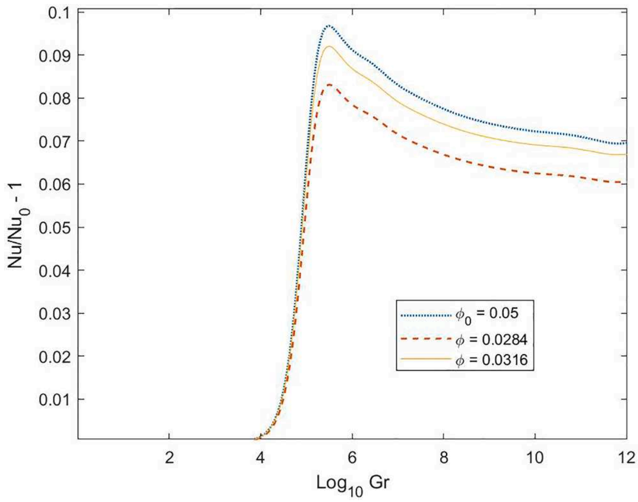

Fig. 12. Additional Nusselt number computed by constant phase fraction simulations with $\phi = 0.0284$ and $\phi = 0.0316$, which bracket $\phi(\overline{T})$ at the low and high Gr values, respectively, for the gas exchange phase fraction model for $\phi_0 = s^*(0^\circ\mathrm{C})\frac{RT}{PM_w} \sim 0.53$. It is observed that the gas exchange model has greater additional heat transfer than any in the range of values used for the constant phase fraction model.

$s^*(0^\circ\mathrm{C})\frac{RT}{PM_w}$. These approximations are extracted by computing *a posteriori* the values of $\phi(\overline{T})$, for the simulations in Fig. 11. As seen in Fig. 12, the gas exchange has greater additional heat transfer than any of the range of average phase fractions – inhomogeneity allows for high heat transfer in through the hot regimes that can compensate for the higher resistance in the colder areas, on average.

Perhaps the major takeaway message is that the trends predicted by the constant microbubble phase fraction all hold with this simplistic treatment of dissolved gas exchange with the microbubble phase, but the overall additional value is diminished relative to the maximum microbubble phase fraction observable at the high temperatures near the hot wall.

3.5. *Assessing the Boussinesq approximation*

The rationale for the original adoption of the Boussinesq approximation is about the intended use of this modelling approach for comparison with experiments. After using the governing equations in [2] for the analysis of the Mpemba and Osborne [1] transient experiments, it is clear that extending these experiments to well controlled, systematically varied microbubble phase fractions, is a straightforward experiment. However, transient buoyant convection is not well studied. Adding compressibility effects to transient buoyant convection introduces sound waves as a mode of momentum transport. Given the speed of sound in water is much more rapid than vortical motions of the liquid, the temporal resolution implications are severe.

In general, numerical analysis that is only concerned with hydrodynamics in liquids excludes sound waves by assuming divergence-free velocity fields as the approximation to the continuity equation. However, adopting the compressible, transient continuity equation, can still be treated by numerical analysis to take hydrodynamic time steps that ignore fast sound wave momentum transport, by implementing stiff solvers, such as Gear's Method, which incorporates backward timestepping (see Cooper, [25]). If stiff systems can be avoided by selection of the model equations, it is preferable to implementing stiff solvers, particularly when the rapid timescale dynamics are of no practical concern, such as sound waves emanating from this liquid-filled cavity.

Table 2
Emergent Nusselt number comparison of the compressible and Boussinesq continuity models for $Gr = 2 \times 10^{11}$.

Model	Nusselt number
Boussinesq	69.2790
Compressible	69.2646

However, the more general compressible continuity equation for the steady state dynamics equations, $\nabla \cdot \widehat{\rho}(T)\boldsymbol{u} = 0$, has no mode for sound wave emission, so the overall PDE system is not stiff. Comsol Multiphysics v.5.6 implements this version of the Navier-Stokes equations as a built-in model variant, readily selected. The Bousinesq approximation (2) and the compressible variant were both simulated on the high resolution mesh described in Table 1, using the parametric solver, from $Gr = 2$ *to* 2×10^{13}, for the base case of no microbubbles.

Table 2 shows the numerical values of the Nusselt number found from the two simulations for the specific case of $Gr = 2 \times 10^{11}$. The difference is in the fourth significant digit, which is barely above the mesh resolution study of Table 1 in precision. There is, however, a noticeable difference in convergence properties of the two classes of simulation. The compressible model and Boussinesq model were similar in computational intensity up to $Gr \sim 10^{12}$ in the parametric continuation approach, taking a similar amount of time, with similar levels of iterations needed for convergence at intermediate *Gr* values. The computational intensity changed dramatically with higher *Gr* numbers. The compressible model achieved the full range in ~9 h on a 6 core Intel i5-8600 K processor at 3.6 GHz with 64 Gb RAM, requiring up to 20 Gb intermediate swell RAM. The Boussinesq model was abandoned at 24 h on the same processor with $Gr \sim 10^{13}$, requiring intermediate RAM swell of ~40 Gb. Many more intermediate iterations of the stiffness matrix were required.

Of course, inspection of Fig. 3 makes clear that at the highest *Gr* values computed, the shear in the thermal boundary layer becomes high and the temperature gradients large, potentially requiring mesh refinement for faster convergence as the boundary layers become even thinner. This insight is not new. A recent review [26] concludes that the Boussinesq equation is an acceptable approximation when the physical and thermodynamic properties of the fluid are permitted to vary with temperature, as is conducted here, by comparison to the weakly compressible and low Mach number approaches reviewed, for buoyant convective flows. For the purposes of the transient extension of the microbubble mediated heat transport model put forth here, the initial *Gr* number should be the main indicator of whether to adopt the Boussinesq approach which is not stiff, or the compressible approach, which has sound waves that add stiffness which would then be treated by a stiff solver to ignore the sound wave dynamics.

4. Conclusions and outlook

The hypothesis of proportionality between the additional heat transfer and the microbubble phase fraction holds within the microfluidic range of flow cells, where convection dominates as proposed in [2] as due to scaling analysis. The prediction is found to hold only closely in the microfluidic regime of steady state buoyant convection. Monotonic increase but less than proportionality holds with larger flow cell characteristic lengths where stable stratification forms under steady state conditions. The formation of the stable stratification dominates the heat transfer dynamics, which could be alleviated by continuous microbubble injection and removal, such as in the airlift loop open system, frequently adopted for bioreactors [13].

The buoyant heat transfer in a slot, with differential vertical side wall heating is a canonical heat transfer mode, and thus widely applied in the initial design phase for heat exchangers. Where the operational fluid is water in such slots, the addition of a long-lived dispersed microbubble phase is predicted by this paper to achieve faster heat transfer rates as proposed by [2] and consistent with accelerations found by [1]. The sole industrial applications currently known to rely on bubbles to mediate heat transfer are direct contact condensers and evaporators [89], but these do not achieve sufficient macromixing within the bubble phase to conduct the additional heat from hot liquid zones to cold liquid zones near the cold wall (e.g. condensers) with fine or coarse bubbles, as demonstrated by [6]. Hence, the immediate obvious application of this study is to direct contact condensers, which likely use water in the non-Boussinesq temperature range as the external cooling liquid.

Including the effect of gas exchange between the microbubble phase and dissolved gases in the liquid, in the most simple treatment – requiring saturation of gases at all temperatures – does not qualitatively change the conclusions that the additional heat transfer at steady state due to microbubbles is linear in the microfluidic regime, and monotonic but diminishing gradually with increase phase fraction for larger domains. This supports the letter of the hypothesis of Zimmerman [2] for the explanation of the Mpemba effect, and is certainly a strong support for the correlation. The microbubble phase fraction is shown to control the additional heat transfer, with increases of 5–45% predicted for the range of phase fractions of 2–20%. With the principle effects of dissolution captured, the above additional heat transfer ranges from 3 to 30%.

It has been noted by several participants of HEFAT 2021 that the Mpemba effect experiments are transient, but the simulations here are steady state. Certainly the extension to transient dynamics for equations (1) and (2) is very simple, although requiring substantial numerical analysis to establish consistent initial conditions. Nevertheless, the Mpemba and Osborne [1] findings show time scales for the onset of solidification of 30–60 min, by which it is simple to echo the observations of Burridge and Linden [4] that pseudo-steady stratifications that are predicted by the steady state simulations for centimetre scale and larger Gr must establish, providing a bottleneck on heat transfer, which becomes boundary layer controlled. Bregovic [24] found similar timescales for experiments with unboiled water, likely saturated in dissolved gases. Nevertheless, transient simulations would allow the assessment of whether microbubble mediation predicts the same scale heat transfer rates for such transient experiments. However, agreement on the appropriate protocols [3] so that our explanation for the origin of the effect is controlled – known microbubble phase fractions – is essential. Desai and co-workers [27,28,29] provide a prescription for estimating microbubble phase fraction by acoustic bubble spectrometry, which should be sufficient for initial state characterization.

Zimmerman [2] identified several potential applications for this particular configuration, including heat storage in water tanks which are subject to buoyant convection alone. The closest to industrial usage are the potential application to desalination [30] or fracking produced water remediation [31], replacing direct contact evaporation and condensation. The latter is incorporated by the MIT spinout company Gradiant, mimicking the environmental desalination by solr heating for evaporation and overnight cooling for condensation. The scale of the parameters matches in all but the bubble phase, where conventional methods use bubbles with diameters 4 mm and larger. The additional convection from phase change only occurs with microbubble convection. It is fitting that the mechanism [23] likely responsible for Mpemba effect [1] rapidly chilling water be used for more sustainable water processing.

Declaration of Competing Interest

The authors declare that they have no known competing financial interests or personal relationships that could have appeared to influence the work reported in this paper.

Acknowledgments

The author acknowledges the Engineering and Physical Sciences Research Council (EPSRC) for supporting this work financially (Grant no. EP/K001329/1, EP/N011511/1 and EP/S031421/1). A preliminary version of this paper was presented and published in the proceedings of the 15th International Conference on Heat Transfer, Fluid Mechanics and Thermodynamics (HEFAT2021), Online, 26 – 28 July 2021, as a keynote address.

References

[1] E.B. Mpemba, D.G. Osborne, Cool? Phys. Educ. 4 (1969) 172–175.
[2] W.B. Zimmerman, Towards a microbubble condenser: Dispersed microbubble mediation of additional heat transfer in aqueous solutions due to phase change dynamics in airlift vessels, Chem. Eng. Sci. 238 (2021) 116618.
[3] W.B. Zimmerman, In search of a Mpemba Effect Protocol: Some hot water does cool and freeze faster than cold, Chem. Eng. Sci. 247 (2022) 117043.
[4] H.C. Burridge, P.F. Linden, Questioning the Mpemba effect: hot water does not cool more quickly than cold, Sci. Rep. 6 (2016) 37665.
[5] D.J. Gilmour, W.B. Zimmerman, Microbubble Intensification of Bioprocessing, Adv. Microb. Physiol. 77 (2020) 1–35.
[6] W.B. Zimmerman, M.K.H. Al-Mashhadani, H.C.H. Bandulasena, Evaporation dynamics of microbubbles, Chem. Eng. Sci. 101 (2013) 865–877.
[7] P.D. Desai, M. Turley, R. Robinson, W.B. Zimmerman, Hot microbubble injection in thin liquid film layers for ammonia separation from ammonia rich-wastewater, Chem. Eng. Process. – Process Intensificat., https://doi.org/10.1016/j.cep.2021.108693.
[8] C.P. Ribeiro, L.P.C. Lage, Experimental study on bubble size distributions in a direct-contact evaporator, Braz. J. Chem. Eng. 21 (1) (2004) 69–81.
[9] C.P. Ribeiro, L.P.C. Lage, Gas-Liquid Direct-Contact Evaporation: A Review, Chem. Eng. Technol. 28 (10) (2005) 1081–1107.
[10] D. Mazumder, A.K. Dikshit, Applications of the deep-shaft activated sludge process in wastewater treatment, Int. J. Environ. Pollut. 17 (3) (2002) 266–272.
[11] W. Fan, P. Desai, W.B. Zimmerman, Y. Duan, J.C. Crittenden, C. Wang, M. Huo, Optical density inferences in aqueous solution with embedded micro/nano bubbles: A reminder for the emerging green bubble cleantech, J. Clean. Prod. 294 (2021) 126258.
[12] U. Ghia, K.N. Ghia, C.T. Shin, High-Re Solutions for Incompressible Flow Using the Navier-Stokes Equations and a Multigrid Method, J. Comput. Phys. 48 (3) (1982) 387–411.
[13] M.K.H. Al-Mashhadani, S.J. Wilkinson, W.B. Zimmerman, Airlift bioreactor for biological applications with microbubble mediated transport processes, Chem. Eng. Sci. 137 (2015) 243–253.
[14] W.B.J. Zimmerman, Multiphysics Modelling with Finite Element Methods, World Scientific Series on Stability, Vibration and Control of Systems, vol. 18, Singapore, 2006.
[15] W.B. Zimmerman, The effect of chemical equilibrium on the formation of stable stratification, Appl. Sci. Res. 59 (1998) 298.
[16] J.S. Turner, Buoyancy effects in fluids, Cambridge University Press, Cambridge, 1979.
[17] H. Otto, C. Cierpka, Influence of thermal stratification on vertical natural convection—Experimental investigations on the example of thermal energy storage systems, Phys. Fluids 33 (2021) 083614.
[18] W.B. Zimmerman, J.M. Rees, Rollover instability due to double diffusion in a stably stratified cylindrical tank, Phys. Fluids 19 (2007) 123604.
[19] H. Watanabe, K. Iizuka, The Influence of Dissolved Gases on the Density of Water, Metrologia 21 (1) (1985) 19–26.
[20] T. Karbowiak, R.D. Gougeon, J.-B. Alinc, L. Brachais, F. Debeaufort, A. Voilley, D. Chassagne, Wine Oxidation and the Role of Cork, Crit. Rev. Food Sci. Nutr. 50 (1) (2009) 20–52.
[21] D. Tromans, Temperature and pressure dependent solubility of oxygen in water: a thermodynamic analysis, Hydrometallurgy 48 (3) (1998) 327–342.
[22] Engineering ToolBox, 2004. *Air Solubility in Water*. [online] Available at: https://www.engineeringtoolbox.com/air-solubility-water-d_639.html (accessed 26 March 2021).
[23] M.Z. Brucker, The Winkler Method - Measuring Dissolved Oxygen, Montana State University, https://serc.carleton.edu/microbelife/research_methods/environ_sampling/oxygen.html, 2021.

[24] N. Bregović, Mpemba effect from a viewpoint of an experimental physical chemist. http://www.rsc.org/learn-chemistry/resource/res00001018/the-mpemba-effect?cmpid= CMP00007615 (Date of access:05/01/2016) (2012).
[25] G.J. Cooper, The numerical solution of stiff differential equations, FEBS Lett. 2 (Supplement) (1969) S22–S29.
[26] P. Mayeli, G.J. Sheard, Buoyancy-driven flows beyond the Boussinesq approximation: A brief review, Int. Commun. Heat Mass Transfer 125 (2021) 105316.
[27] P. Desai, W. Ng, M. Hines, Y. Riaz, V. Tesar, W. Zimmerman, Comparison of Bubble Size Distributions Inferred from Acoustic, Optical Visualisation, and Laser Diffraction, Colloids Interfaces 3 (4) (2019) 65.
[28] P.D. Desai, PhD thesis, University of Sheffield, 2017.
[29] P. Desai, M. Hines, Y. Riaz, W. Zimmerman, Resonant Pulsing Frequency Effect for Much Smaller Bubble Formation with Fluidic Oscillation, Energies 11 (10) (2018) 2680.
[30] M.J. Francis, R.M. Pashley, Thermal desalination using a non-boiling bubble column, Desalin. Water Treat. 12 (1-3) (2009) 155–161.
[31] G.P. Narayan, M.H. Sharqawy, E.K. Summers, V.J.H. Lienhard, S.M. Zubair, M. A. Antar, The potential of solar-driven humidifcation–dehumidifcation desalination for smallscale decentralized water production, Renew. Sust. Energy Rev. 14 (2010) 1187–1201.